Controlling phonon lifetimes via sublattice disordering in $AgBiSe_2$

J. L. Niedziela*

Materials Science and Technology Division, Oak Ridge National Laboratory, Oak Ridge, TN 37831, USA

Department of Mechanical Engineering and Materials Science, Duke University, Durham, NC 27708, USA and

Nuclear Nonproliferation Division, Oak Ridge National Laboratory, Oak Ridge, TN 37831, USA

D. Bansal, J. Ding, and T. Lanigan-Atkins

Department of Mechanical Engineering and Materials Science, Duke University, Durham, NC 27708, USA

C. Li

Materials Science and Engineering, Department of Mechanical Engineering, University of California, Riverside, CA 92521, USA

A. F. May and H. Wang

Materials Science and Technology Division, Oak Ridge National Laboratory, Oak Ridge, TN 37831, USA

J. Y. Y. Lin, D. L. Abernathy, G. Ehlers, and A. Huq

Neutron Scattering Division, Oak Ridge National Laboratory, Oak Ridge, TN 37831, USA

D. Parshall and J. W. Lynn

NIST Center for Neutron Research, National Institute of Standards and Technology, Gaithersburg, MD, 20899, USA

O. Delaire†

Department of Mechanical Engineering and Materials Science, Duke University, Durham, NC 27708, USA and

Department of Physics and Department of Chemistry, Duke University, Durham, NC 27708, USA

(Dated: August 20, 2020)

Abstract

Understanding and controlling microscopic heat transfer mechanisms in solids is critical to material design in numerous technological applications. Yet, current understanding of thermal transport in semiconductors and insulators is limited by the difficulty in directly measuring individual phonon lifetimes and mean free paths, and studying their dependence on the microscopic state of the material. Here we report our measurements of microscopic phonon scattering rates in $AgBiSe_2$, which exhibits a controllable, reversible change directly linked to microstructure evolution near a reversible structural phase transition, which directly impacts the thermal conductivity. We demonstrate a step-like doubling of phonon scattering rates resultant from the cation disordering at the structural transition. To rationalize the neutron scattering data, we leverage a step-wise approach to account for alterations to the thermal conductivity that are imparted by distinct scattering mechanisms. These results highlight the potential of tunable microstructures housed in a stable crystal matrix to provide a practical route to tailor phonon scattering to optimize thermal transport properties.

INTRODUCTION

Gaining a microscopic understanding of heat transfer processes is critical for rationally designing materials in numerous technological applications, including thermoelectrics, thermal barrier coatings, semiconductors for microelectronics, and nuclear fuel. Thermoelectric materials enable direct conversion of thermal gradients into electrical energy, and are sought in applications using natural or man-made heat sources[1–6]. Thermoelectric conversion efficiency is characterized by a figure of merit $zT = \alpha^2\sigma T/\kappa_{tot}$, where α is the Seebeck coefficient, σ is the electrical conductivity, and $\kappa_{\rm tot}$ is the overall thermal conductivity of the material, itself the sum of lattice and electronic contributions, $\kappa_{\rm tot} = \kappa_{\rm lat} + \kappa_{\rm el}$. This has prompted wide-ranging efforts to maximally suppress phonon propagation while preserving electronic mobility to maintain a high power factor $\alpha^2\sigma$. Yet, while critical to benchmark phonon scattering theories, the experimental assessment of the lifetimes of individual phonon modes –in a momentum and energy resolved fashion– and their evolution as a function of temperature or sample conditions, remains very challenging.

Semiconductors of the type ABX_2 (group I-V-VI_2) have previously been shown to exhibit an intrinsically low lattice thermal conductivity, while achieving competitive power factors[7–9]. Examples include $AgBiSe_2$ $NaSbSe_2$, $NaBiTe_2$, $NaSbTe_2$, as well as $AgSbTe_2$, which has also successfully been alloyed with PbTe in the so-called LAST compound [10]. $AgBiSe_2$ is a promising thermoelectric material with zT approaching 1 near 800 K for n-type samples[11, 12], and 1.5 at 750 K for nanostructured p-type samples[13], and potential for room temperature application[14]. The structure easily allows for doping and substitution, enabling tuning of transport properties[11–13, 15, 16].

The microscopic origin of the very low thermal conductivity in the I-V-VI_2 semiconductors remains controversial. For example, Morelli *et. al.*[8] argued that anharmonic phonon–phonon scattering was the dominant scattering mechanism in $AgSbTe_2$ and that the temperature independent $\kappa_{\rm lat}$ would arise as a consequence of such a strong anharmonicity that the material was reaching the minimum possible thermal conductivity at all temperatures[8]. In contrast, neutron scattering investigations on $AgSbTe_2$ linked the observed T-independent phonon scattering rates to the emergence of a spontaneous nanostructure with short-range ordering on the cation sublattice[17–19], also observed by electron microscopy and scanning probe studies [20–23].

Although $AgSbTe_2$ exhibits cation short-range ordering on a pseudo–rocksalt lattice at all temperatures [17, 18], $AgBiSe_2$ can be tuned with heat treatments to exhibit either disordered or

long-range ordered cations while preserving the crystallinity [15, 24]. Thus, $AgBiSe_2$ provides a rare opportunity to directly investigate the role of cation disordering on the phonon scattering rates in a semiconductor, by probing the dynamic behavior across the order–disorder transition. Here, we examine the phonon scattering mechanisms in $AgBiSe_2$ using neutron scattering, thermal diffusivity measurements, and first-principles calculations to understand the connection with the structural evolution. In particular, we performed inelastic neutron scattering (INS) measurements on large single-crystals to extract quantitative information about the scattering rates, focusing on the transverse acoustic phonons that dominate the thermal conductivity.

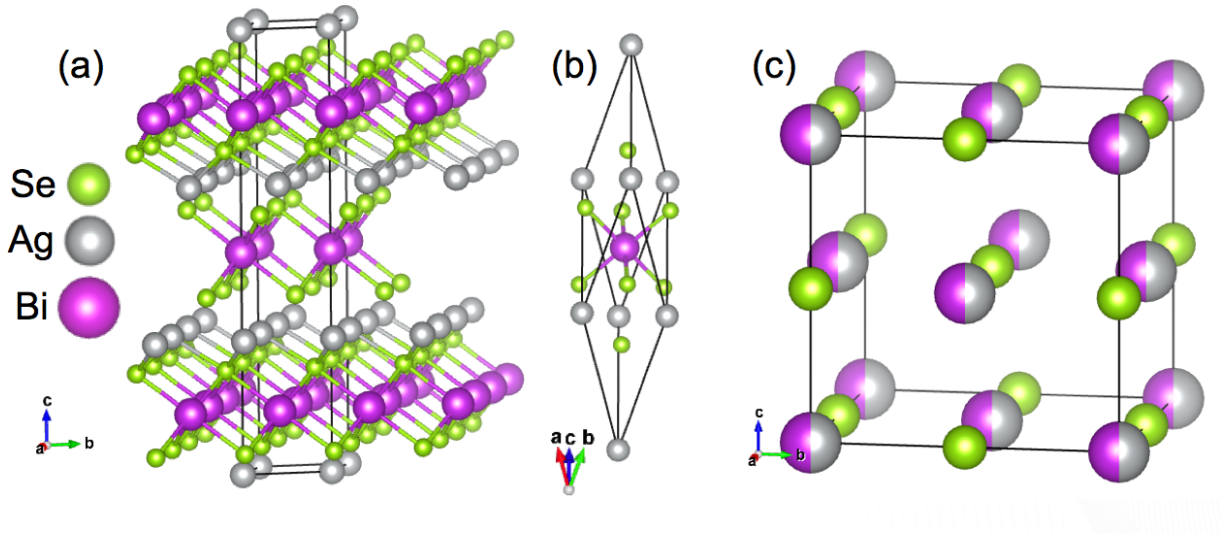

FIG. 1. (color) Structure evolution of $AgBiSe_2$. (a) Low-temperature ($T \leq 390\ K$) α-phase. The Se layers alternate with layers of Bi and Ag. (b) Intermediate temperature ($393 \leq T \leq 560$ K) β phase, which is a slightly distorted rhombohedral modification of the α phase. (c) High-temperature rock salt γ phase, stable for $T \geq 560\ K$, exhibiting a disordered distribution of Ag^{+} and Bi^{3+} on the cation sublattice. The rock salt cubic $\langle 111 \rangle$ directions yield the rhombohedral/hexagonal axes of β/α domains at low T.

$AgBiSe_2$ possesses three different crystalline phases depending on temperature[24, 25], with distinct orderings of cations, as shown in Fig. 1. The high-symmetry rock-salt cubic γ-phase ($Fm\bar{3}m$, SG-225) is observed for $T \geq 560$ K (Fig. 1c), with Ag^{+} and Bi^{3+} cations randomly distributed on a face-centered cubic (FCC) sublattice and Se anions on their separate FCC sublattice. Between 393 and 560 K, the system adopts a rhombohedral β-phase ($R\bar{3}m$, SG-166), with segregation of the Ag and Bi ions into the $(111)_{\text{cubic}}$ planes of the high-temperature γ-phase (Fig 1b). The low-temperature α-phase below 393 K, shown in Fig. 1a, is hexagonal ($P\bar{3}m1$, SG-164), with

Ag and Bi layers slightly displaced along the c-axis (along to $\langle 111 \rangle_{\text{cubic}}$) compared with the β-phase[25, 26]. The FCC sublattice of Se from the rock-salt γ-phase is preserved through these phase transitions, but with slight distortions. Earlier transmission electron microscopy (TEM) work[24], showed that the microstructure of the room temperature and intermediate phases is comprised of twinned domains with different orientations of the rhombohedral/trigonal axis, corresponding to Ag/Bi layers orthogonal to different $\langle 111 \rangle_{\text{cubic}}$ directions. The twin domains in that study had a typical size of 50-100 *nm*, with a twinning microstructure expected to be dependent on thermal history.

The disordered rock-salt phase of $AgBiSe_2$ can be quenched after high temperature annealing. This method was used for the TEM study in Ref.[24] and to compare the lattice thermal conductivity of the cubic and trigonal phases at cryogenic temperatures in polycrystalline material[9]. Lattice thermal conductivity measurements conducted this way are drastically different between trigonal $AgBiSe_2$, which displays $\kappa_{\text{lat}} \sim T^{-1}$ characteristic of anharmonic scattering above a maximum at $T \sim 30\,\text{K}$, and the quenched rock-salt $AgBiSe_2$ phase, which displays a glass-like, T-independent κ_{lat} between 10 and 300 K[9]. The thermal conductivity of quenched rock-salt $AgBiSe_2$ is similar to that of rock-salt $AgSbTe_2$[9]. The annealed, long-range ordered low-symmetry phase has larger thermal conductivity than the quenched phase at temperatures up to 300 K[9]. Thus, the degree of cation ordering is an effective way of controlling thermal conductivity in this system. While polycrystalline $AgBiSe_2$ can be quenched to retain the rock-salt disordered phase, single-crystals shatter upon quenching, thus we studied cation disordering on heating across the ordered rhombohedral to disordered rock-salt transition instead.

INS is a powerful experimental probe of phonons in materials. While optical spectroscopies provide high-resolution phonon spectra, they are limited to modes at (or near) the Brillouin zone center and are limited by selection rules. In contrast, INS can access phonon modes across the entire Brillouin zone, with energy, momentum, and eigenvector polarization selectivity. By combining measurements of powder and single-crystal samples, we probed both the phonon density of states (DOS), as well as the temperature dependent phonon dispersions and linewidths, and correlate our results with the structural evolution obtained from neutron diffraction.

Linewidths derived from INS measurements provide critical information about phonon scattering processes. Nevertheless, few INS investigations of phonon linewidths in thermoelectrics have been reported to date [17, 18, 27, 28] because of the technical challenges of obtaining large single-crystals, and the expertise needed for accurate corrections of complex resolution effects.

For $AgBiSe_2$, the energy width of the transverse acoustic phonons are sufficiently broad that we can quantitatively extract linewidths along extended portions of the dispersion. To this end, we performed Monte Carlo modeling of the instrument resolution function[29] to deconvolve the it from the linewidth.

Further, we exploit first-principles calculations to rationalize the phonon scattering mechanisms. Phonon simulations were done on several structures to evaluate effects of cation ordering on phonon dispersions and thermal conductivity and aid INS interpretation. To understand the effect of cation ordering on phonon dispersions and the dynamical structure factor, we considered two variants of alloy structures including cubic D_4 and trigonal $L1_1$[30]. Additional simulations were performed for the disordered γ-phase using a virtual crystal approximation (VCA) based on the rock-salt PbSe structure but using the average mass of Ag and Bi on the cation site and including effects of point-defect scattering. Thus, we determine the relative influence of anharmonic processes, mass disorder, and short-range ordering on phonon scattering rates, to account for the low thermal conductivity of $AgBiSe_2$.

METHODS

Single crystal inelastic neutron scattering

For neutron scattering by harmonic phonons, which have infinitely long lifetimes, the coherent cross section for one-phonon emission is given by [31]:

$$\left(\frac{d^2\sigma}{d\Omega dE}\right)_{coh} = \frac{k'}{k}\frac{(2\pi)^3}{2v_0}\Sigma_s\Sigma_\tau\frac{1}{E_s} \left|\Sigma_d\frac{\overline{b_d}}{\sqrt{M_d}}\exp(-\mathrm{W_d})\exp(\mathrm{i}\mathbf{Q}\cdot\mathbf{d})(\mathbf{Q}\cdot\mathbf{e_{ds}})\right|^2 \times\langle n_s+1\rangle\delta(E-E_s)\delta(\mathbf{Q}-\mathbf{q}-\tau) = \frac{\sigma_{coh}}{4\pi}\frac{k'}{k}NS(\mathbf{Q},E), \quad (1)$$

where k', k are the final and incident neutron wave vector, $\mathbf{q}$ the phonon wave vector, E_s the eigenvalue of the phonon corresponding to the branch index s, $\mathbf{e_{ds}}$ is the phonon eigenvector, τ is the reciprocal lattice vector, d the atom index in the unit cell, $\mathbf{d}$ is the atomic position in the unit cell, $\overline{b_d}$ is the average scattering length for atom d, M is the atomic mass, W the corresponding Debye-

Waller factor, $\mathbf{Q}$ the wave vector transfer, and $S(\mathbf{Q},E)$ the dynamical structure factor. Phonon scattering processes lead to finite lifetimes, $\tau_{\mathbf{q},j}$, and as a consequence the phonon spectral functions $A_{\mathbf{q},j}(E)$ are no-longer δ functions, but acquire a finite energy width (linewidth). [32–35] In the weak scattering regime, the phonon spectral function can be described by a Lorentzian function, and the full-width at half-maximum provides a measure of the mode-resolved scattering rate, $\tau^{-1}_{\mathbf{q},j}$ [33]. The dynamical susceptibility $\chi^{''}(\mathbf{Q},E)$ can be derived from $S(\mathbf{Q},E)$ following:

$$\chi^{''}(\mathbf{Q},E) = (1-\exp\{-\mathrm{E}/\mathrm{k_B T}\})\mathrm{S}(\mathbf{Q},\mathrm{E}), \tag{2}$$

where E is the energy, k_B is the Boltzmann constant, and T is the temperature of the measurement.

We used high-quality single-crystals (mass $\sim$ 8 g), grown with a modified Bridgman methods (details in ESI[36]) and annealed ex-situ in the α phase for three weeks. All experiments were performed on this crystal, using the thermal triple-axis spectrometer BT-7 at the NIST Center for Neutron Scattering[37], the Wide Angular Range Chopper Spectrometer (ARCS) [38], and the Cold Neutron Chopper Spectrometer (CNCS) [39], time-of-flight chopper spectrometers at the Spallation Neutron Source, in that order. While the cation transition is reversible, in-situ heating cycles between the α and γ phases during multiple INS measurements could affect the sample microstructure, as it is not possible to anneal *in-situ* as long as during sample preparation. For this reason, a second crystal, annealed *ex-situ* in the α-phase, was measured (CNCS) for comparison with the first crystal having undergone several *in-situ* temperature cycles (BT-7, ARCS, CNCS). Our measurements show that the phonon spectra were not substantially affected by *in-situ* thermal cycling.

For all INS measurements, crystals were mounted in the (HHL) scattering plane (pseudocubic notation) to provide access to high symmetry directions. Scans of phonons were conducted at temperatures ranging between 50 K and 690 K on BT-7. For the ARCS and CNCS measurements, the sample was mounted in a closed-cycle displex and measured at at 300 K and 640 K. At ARCS, the selected incident energy of 25 meV provided elastic line energy resolution of 1.6 meV decreasing to 1.3 meV at 5 meV energy transfer[40], and a rotating collimator was used to reduce the scattering background[41, 42]. For the CNCS measurements, an incident energy of 15 meV was used, which provides an estimated elastic line energy resolution of 0.7 meV and 0.4 meV at 5 meV energy transfer. For TOF INS measurements, the crystal was rotated through a large angular range in 1 degree steps, mapping the four-dimensional $S(\mathbf{Q},E)$ for a large number of Brillouin zones. Data were reduced using Mantid algorithms[43], and analyzed using HORACE[44], These

single-crystals measurements enabled detailed investigation of both low-energy phonons and elastic scattering. Further details of INS experiments including temperature correction information are provided in the ESI[36].

Powder INS

For single-phonon scattering in a polyatomic material, the inelastic neutron scattering cross-section is proportional to the scattering function, which is closely related to the phonon DOS in the case of incoherent scattering:

$$S_{\text{inc}}(\mathbf{Q},E) = \sum_i \sigma_i \frac{\hbar^2 Q^2}{2M_i} \exp(-2W_i) \frac{g_i(E)}{E} [n_T(E)+1], \tag{3}$$

where $\mathbf{Q}$ and E are the momentum and energy transfer to the sample, $Q = |\mathbf{Q}|$, σ_i, M_i, and $\exp(-2W_i)$ are the neutron scattering cross-section, mass, and Debye-Waller factor for atom i, respectively, and $n_T(E)$ is the Bose occupation factor[31].

The partial phonon DOS, g_i, is defined as

$$g_i(E) = \sum_{j,\boldsymbol{q}} |e_i(j,\boldsymbol{q})|^2 \delta[E - E(j,\boldsymbol{q})], \tag{4}$$

where $E(j,\boldsymbol{q})$ and $e(j,\boldsymbol{q})$ are the phonon energies and eigenvectors [31, 45]. As can be seen from Eq. 3, the measured INS signal (in the incoherent approximation) provides a neutron-weighted approximation to the DOS, with the spectral contributions from each species i corresponding to its partial phonon DOS g_i, weighted with $\exp(-2W_i)\sigma_i/2M_i$. The Debye-Waller factors for each species are close to unity, however, the ratios of neutron cross-sections and masses substantially differ: 0.046 for Ag, 0.0438 for Bi, and 0.105 for Se, making contributions from Se motion dominant in the neutron-weighted DOS.

To determine the DOS, time of flight INS data were collected on a 8 gram powder sample of $AgBiSe_2$ using ARCS[38, 46]. The sample had been annealed for 72 hours prior to the measurements, providing access to the long-range ordered low-temperature phase. Data were collected with incident neutron energies $E_i = 15$ and 40 meV. At $E_i = 40$ meV, the estimated energy resolution at the elastic line (zero energy transfer) was 2.5 meV, which decreases to 0.7 meV at 18 meV. A background measurement from an empty Al can was measured in identical conditions. The data were reduced using Mantid algorithms [43] and analyzed in the incoherent approximation to

obtain the phonon DOS, following a standard procedure[47]. Data are then corrected for neutron weighting effects, as described in the ESI.

Time of Flight Neutron Powder Diffraction

Time-of-flight neutron diffraction data were obtained using the POWGEN instrument[48] at the Spallation Neutron Source. The temperature evolution of the structure and the effect of disordering was studied from 100-600 K. Lattice parameters were extracted from LeBail and Rietveld refinements performed with GSAS[49]. Additional data and temperature correction information are discussed in the ESI.

First-principles simulations

Phonon simulations were performed on several structure variations of $AgBiSe_2$ to evaluate effects of cation ordering on the phonon dispersions and thermal conductivity. First-principles simulations were performed in the framework of density functional theory (DFT) as implemented in the Vienna *ab initio* Simulation Package (VASP 5.3) [50–52]. We used $6 \times 6 \times 6$ Monkhorst-Pack electronic k-point mesh with a plane-wave cut-off energy of 300 eV in all of our simulations. The convergence criteria for the electronic self-consistent loop was set to 10^{-8} eV. The projector-augmented-wave potentials explicitly included 11 valence electrons for Ag, five for Bi, and six for Se. We used both the local density approximation (LDA) [53] and the Perdew-Burke-Ernzerhof (PBE) [54] for the exchange correlation functional. During the relaxation of the structure, the lattice parameters and atomic positions were optimized until forces on all atoms were smaller than 1 meV $Å^{-1}$. We considered two variants of alloy structures D_4 (also known as AF-IIb, space group # 227)[30], and $L1_1$ (also known as AF-Ib, space group # 166) to describe the Ag/Bi ordering as shown in SFig. 1. Due to the difficulty in capturing the site-disordering of the Ag-Bi atoms induced by the phase transition, we use these two variants to assess changes in the phonon dispersion relations induced by different local orderings of cations. Further simulations were performed on the VCA of the rock-salt phase.

For all phases, phonon dispersions were calculated in the harmonic approximation, using the finite displacement approach as implemented in Phonopy[55]. The atomic displacement amplitude was 0.01 Å. Both LDA and PBE calculations resulted in stable phonons, albeit with slightly higher

energies for modes calculated with LDA, which is consistent with the smaller lattice parameter obtained for the structure during relaxations when using the LDA functional.

Thermal transport characterization

Flash thermal diffusivity was used to characterize thermal conductivity above room temperature. The experimental thermal conductivity is calculated as $\kappa = \rho C_p D$ where the ρ, C_p and D are the density, heat capacity and thermal diffusivity. Thermal diffusivity measurements were performed with a Netzsch LFA-457 laser flash apparatus from 300 - 700 K, on an annealed slice cut from a polycrystalline ingot.

RESULTS

We start with a discussion of the phonon behaviors from the temperature-dependent INS measurements. An overview of the dispersions determined with TOF-INS and DFT calculations convoluted with the experimental energy resolution and neutron weighting[56] are provided in Fig. 2, experimental results from TAX-INS in Fig. 3, and the phonon DOS from experiment and calculation in Fig. 4.

The acoustic branches of $AgBiSe_2$ are similar in energy and shape to those measured in $AgSbTe_2$[17, 18], with the $[1,1,0]$-polarized TA branch propagating along $[0,0,1]$ reaching up to ~ 4.7 meV at the zone boundary at 300 K (Fig. 2a), and the $[0,0,1]$-polarized TA branch along $[1,1,0]$ reaching around 6 meV at the top at 300 K (Fig. 3d and Fig. 2b). The top of the longitudinal acoustic (LA) modes is difficult to discern owing to their broadening and merging with optical modes.

The optical modes in $AgBiSe_2$ extend up to ~ 22 meV at 300 K, as seen in the phonon DOS (Fig. 4)e, while the DOS only reaches about 20 meV in $AgSbTe_2$ at the same temperature. This can be explained by the lighter mass of Se compared with Te. In addition, in $AgBiSe_2$ the acoustic modes, below 12 meV, are better separated from the optic modes (spectral peak at $15 < E < 22$ meV in the DOS) than in $AgSbTe_2$, which exhibits a large peak of mixed nature in the DOS at ~ 13 meV. This arises from the larger mass ratio between cations and anions in $AgBiSe_2$. Well defined phonon peaks are seen at 7, 10, 17, and 20 meV in the measurement at 50 K. With increasing temperature, all the features in the DOS tend to broaden, and a distinct shift to lower energy

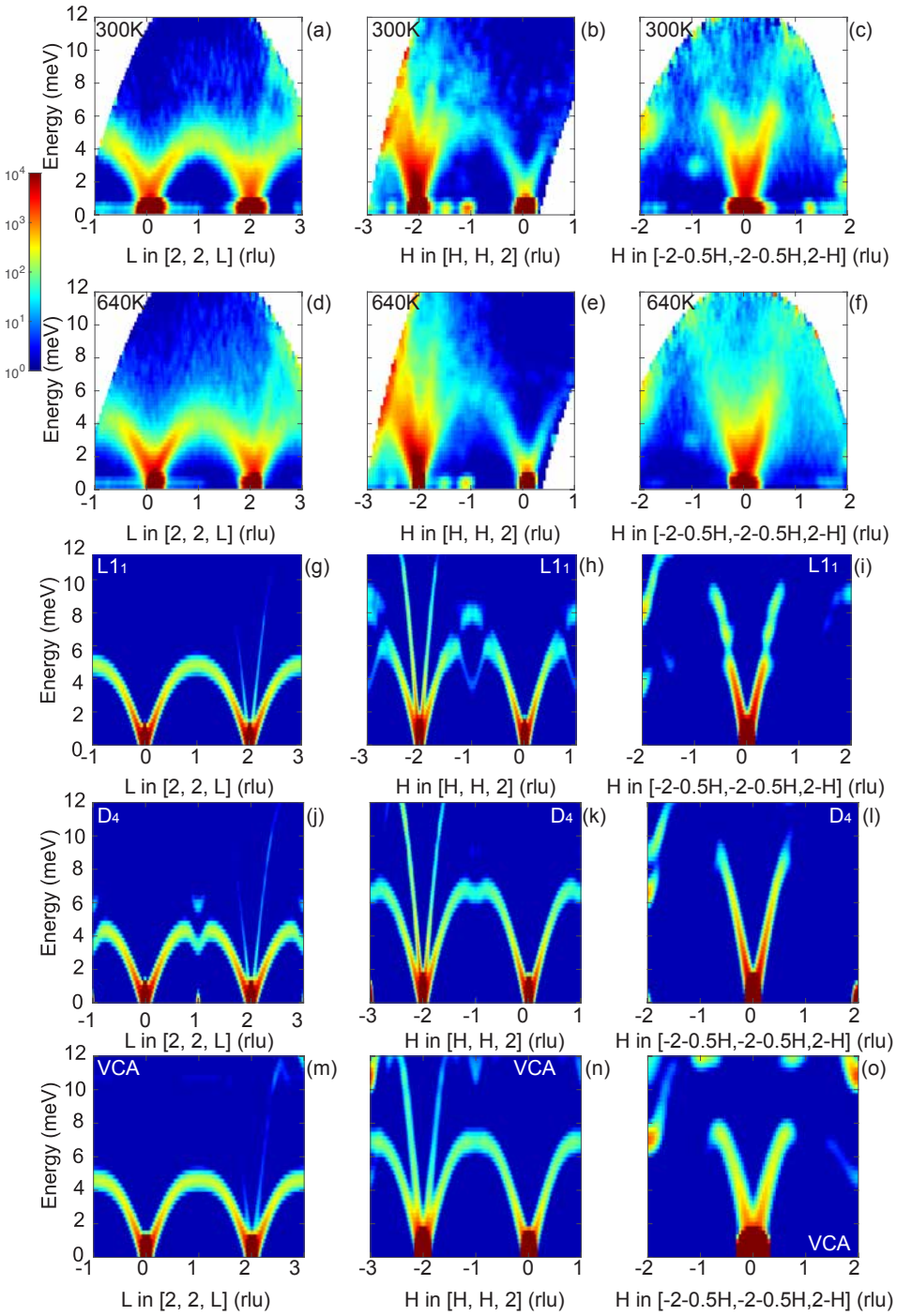

FIG. 2. (color) Dynamic susceptibility $\chi''(\mathbf{Q},E)$ of $AgBiSe_2$ measured at 300 K (a-c) and 640 K (d-f) with CNCS, along reciprocal space directions: (a,d) $(2,2,0)+(0,0,\xi)$, (b,e) $(0,0,2)+(\xi,\xi,0)$, and (c,f) and (-2,-2,2) + $(-0.5\xi,-0.5\xi,-\xi)$. Scattering intensity maps are obtained by integrating in $\pm$ 0.1 *rlu* in orthogonal directions. (g-o) Simulated $\chi''(\mathbf{Q},E)$ along corresponding directions, for the $L1_1$ (g,h,i), D_4 (j,k,l) ordered structures, and a VCA structure (m, n, o). The VCA model is based on rock salt PbSe, replacing the mass of Pb with the average mass of Ag and Bi. In all panels, the logarithmic intensity scale spans four orders of magnitude.

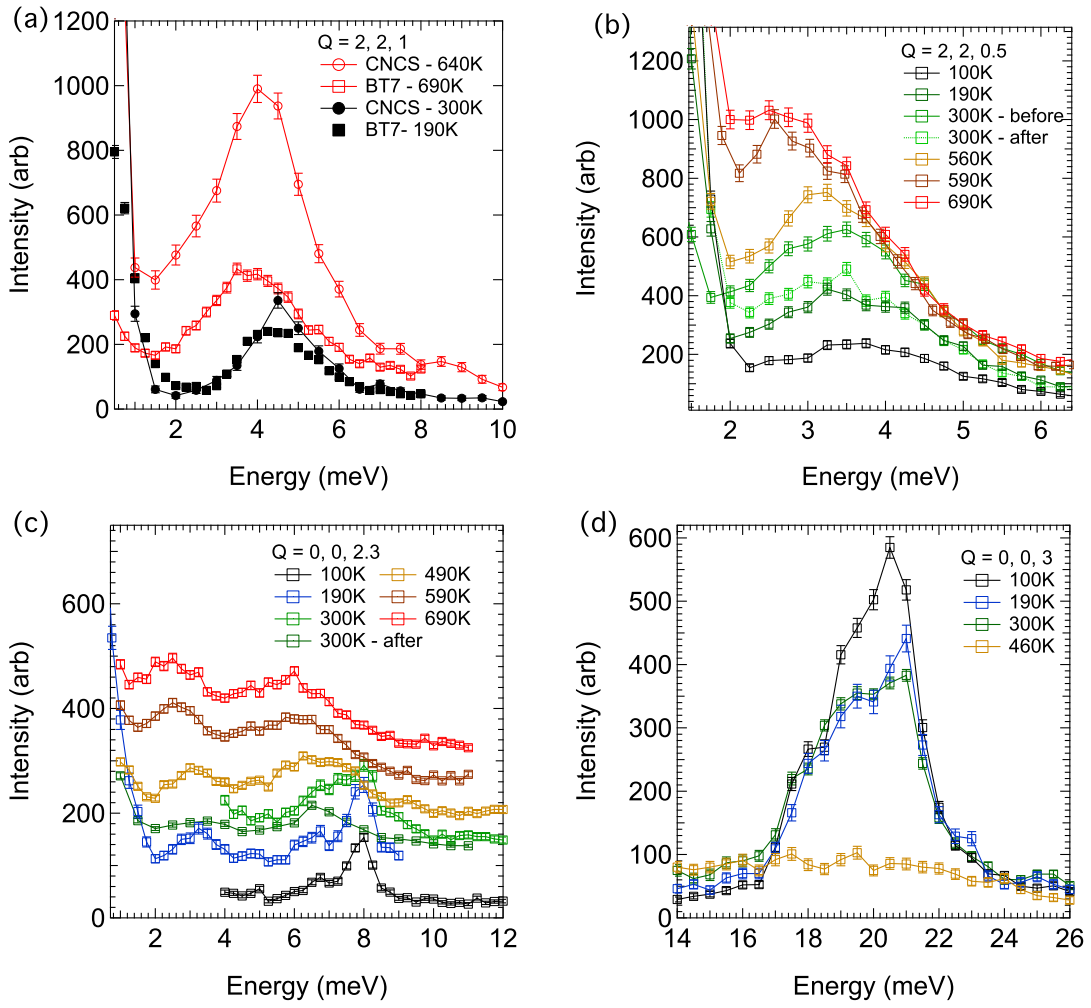

FIG. 3. (color) Representative constant-Q data for $AgBiSe_2$. (a) S(E) for scans at **Q** = (2, 2, 1) showing the softening and broadening on warming of the transverse acoustic mode at the Brillouin zone boundary. (b) S(E) for scans at **Q** = (2, 2, 0.5) showing the softening of the transverse acoustic mode near the Brillouin zone midpoint. (c)Temperature evolution for **Q**=(0,0,2.3) showing a longitudinal optic mode and parasitic transverse mode, which both show broadening on warming. (d) longitudinal acoustic mode at **Q**=(0,0,3) showing the complete damping of high energy optical modes in the β phase.

("softening") can be observed for higher energy peaks.

We now discuss the temperature dependence of the thermal diffusivity and INS measurements. Diffusivity results shown in Fig. 5 reflect a gradual decrease on heating from 300 to 500 K, consistent with increased anharmonic phonon scattering, with little change across the $\alpha - \beta$ transition, as expected considering the limited structural change between these two phases, and their compatible domain structures[24]. On the other hand, a strong suppression of the diffusivity is observed

from the β to the γ phase across $T_{\rm od}$. While the origin of the spike at 525 K is not obvious, a clear step-like drop is observed across the disordering process at $\sim$ 550 K, qualitatively consistent with reports on annealed samples[9]. The diffusivity at room temperature at the end of the cooling cycle is 15% lower than the original starting value, reflecting s strong thermal hysteresis, likely resulting from partial quenching of the disordered γ phase.

The rhombohedral transition appears to depress the number of phonon modes near 10 meV reflected by the decreasing DOS weight near 10 meV, while the transition to the γ phase results in the broadening of the high energy modes involving Se, merging the peaks at 17 and 20 meV. Nevertheless, the mean energy of the DOS remains approximately constant. The average phonon energy $\langle E \rangle$ is obtained from the neutron-deweighted DOS (Fig. 4), and at 50 K and 640 K, we find $\langle E \rangle$ = 13.6 and 12.8 meV, respectively, corresponding to Debye temperatures of 210$\pm$2 and 198$\pm$2 K. This relatively small change indicates little change in the overall bonding strength and resulting force-constants across this temperature range.

We note that the $\beta \rightarrow \gamma$ phase transition is reflected quite strongly in the momentum-resolved phonon measurements. Both the TA and LA phonons in $AgBiSe_2$ experience substantial softening and linewidth broadening with increasing temperature prior to the transition, with a sharp increase in the phonon linewidths at the structural transition. Representative constant-Q scans from INS are shown in Fig. 3. Figures 3a, b show the behavior of the transverse acoustic mode at (a) the Brillouin zone boundary along the $\Gamma - X$ direction, and (b) temperature evolution at the midpoint in that direction. A drastic broadening of optical modes on heating from the $\alpha \rightarrow \beta$, and $\beta \rightarrow \gamma$ phases is particularly notable. Fig. 3c,d show longitudinal scans at $\mathbf{Q} = (0,0,2.3)$, an intermediate location along the $\Gamma - X$ direction, and $\mathbf{Q} = (0,0,3)$, corresponding to the Brillouin zone boundary along $\Gamma - X$. Figure 3d shows a well-defined LO mode at $\sim$ 20 meV for $T < 300$ K, an energy in good agreement with our LDA simulations and the top of the measured phonon DOS. Strikingly, this mode essentially disappears at $T = 460$ K (β phase). Similarly, the LA mode at $\mathbf{Q} = (0,0,2.3)$ shows a well-defined peak at 8 meV in scans at $T = 100, 190, 300$ K in the annealed α phase, but it becomes drastically broader on heating into the β and γ phases. Its energy also drops considerably, from 8 meV to 7 meV across the $\alpha \rightarrow \beta$ transition, and further from 7 meV to 6 meV across $\beta \rightarrow \gamma$ ($T \geqslant 560$ K). The TA mode at about 3 meV is parasitically seen in this longitudinal scan, and its energy is seen to decrease with increasing T as well, but this scattering condition cannot resolve the TA linewidth appropriately. We note that upon cooling back to room temperature in-situ , the LA mode remains broad, and centered at $\sim$ 6.5 meV, which indicates that the cation disorder is likely

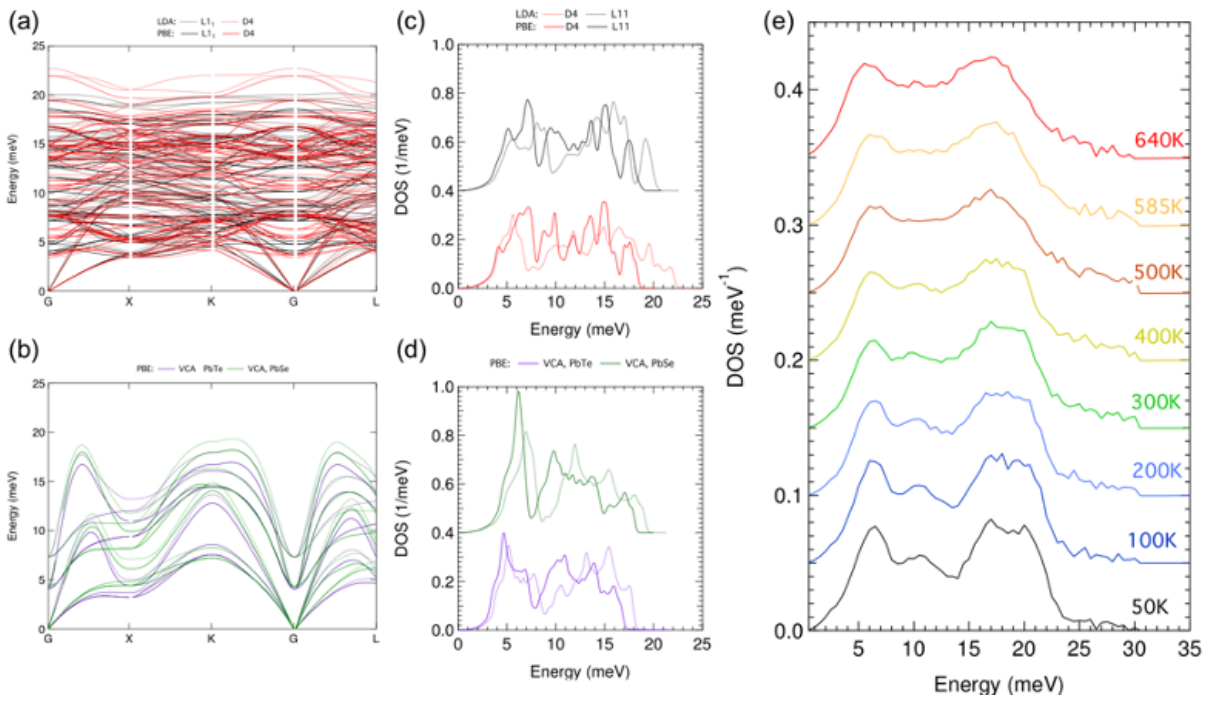

FIG. 4. (color) (a) phonon dispersions calculated from alloy variant structures (b) phonon dispersions of PbSe and PbTe(c) DOS calculated for alloy variants (d) DOS calculated for PbSe and PbTe (e) Neutron deweighted phonon DOS on heating from 10 - 640 K. In (a-d) solid lines correspond to values determined using PBE, while dotted lines correspond to values determined using LDA.

partly quenched, and corroborates strong thermal hysteresis observed in diffusivity measurements (Fig. 5).

Maps of $S(\mathbf{Q},E)$ obtained from CNCS on the crystal previously measured with BT-7 are shown in Fig. 2(a-f) for the reciprocal space directions (22ξ), $(\xi\xi 2)$, and (1,1,-1) + $(\xi\xi\xi)$, at 300 K and 640 K. A softening of the phonon dispersions is readily visible in Fig. 2, and the broadening of the phonon peaks is most apparent along the $[2,2,L]$ direction. Further $S(\mathbf{Q},E)$ maps obtained from measurements with ARCS, covering a wider range of phonon energies, are shown in SFig. 5, showing substantially reduced intensity in the optical modes. Figure 2 also shows comparisons between the INS data and the $S(\mathbf{Q},E)$ calculated from our DFT simulations of phonons for different ordered structures ($L1_1$, D_4), as well as the VCA based on the rock-salt model of the disordered γ phase. Agreement between the experimental data and simulations is reasonable (Fig. 2), with simulations slightly underestimating the TA phonon frequencies, as evident in the comparison of the calculated phonon DOS to the experimentally derived values shown in Fig. 4.

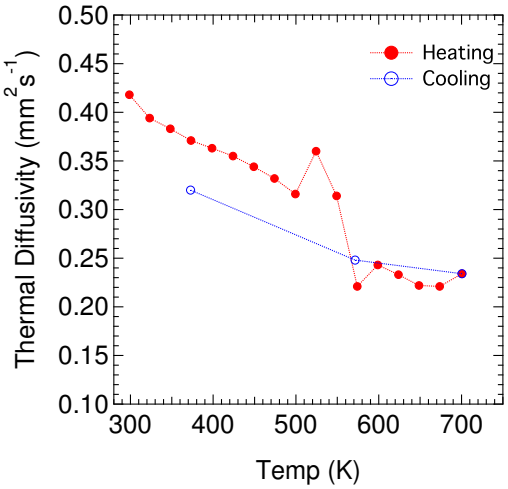

FIG. 5. (color) Thermal diffusivity obtained on heating (red) and cooling (blue).

The acoustic branch intensities and energies along the three directions shown in Fig. 2 are faithfully reproduced overall. Changes in the TA dispersion along $[H,H,2]$ are seen between 300 K and 640 K. Two modes are seen near $H=-1$ at 5.5 meV and 8 meV at 300 K, owing to a low-energy transverse optic branch. The intensity pattern is better reproduced by the $L1_1$ simulation, which features alternate layers of Ag and Bi cations, than by the cubic D4 structure. This feature is clearly associated with cation ordering, as it disappears in the INS data for the γ-phase at 640 K, in good agreement with the rock-salt VCA simulation. This confirms the observation in BT-7 data of the disappearance in the γ-phase of some optic modes associated with the cation ordering (Fig. 3a). The 300 K INS data along $[2,2,L]$ also agree better with the $L1_1$ model than the D4 simulation (no dip in TA mode near $L=1$).

From single-crystal INS data, we extracted the phonon linewidths after corrections for instrument resolution effects.

The results for the intrinsic energy and **Q** resolution for the CNCS spectrometer along high symmetry paths for the transverse acoustic modes in $AgBiSe_2$ propagating along $\Gamma\rightarrow X$, and $\Gamma\rightarrow K$ were calculated using the Monte Carlo (MC) simulation and instrumental settings. BT-7 resolution was modeled using the Popovici method [57] using Reslib as implemented in ResLibCal[58] with the appropriate instrument configuration. Additional details on the resolution modeling are given in the ESI.

We now present the temperature dependence of the phonon energy and linewidth of the TA mode at **Q** = (2,2,1). In the cubic description, this wave vector corresponds to the zone boundary

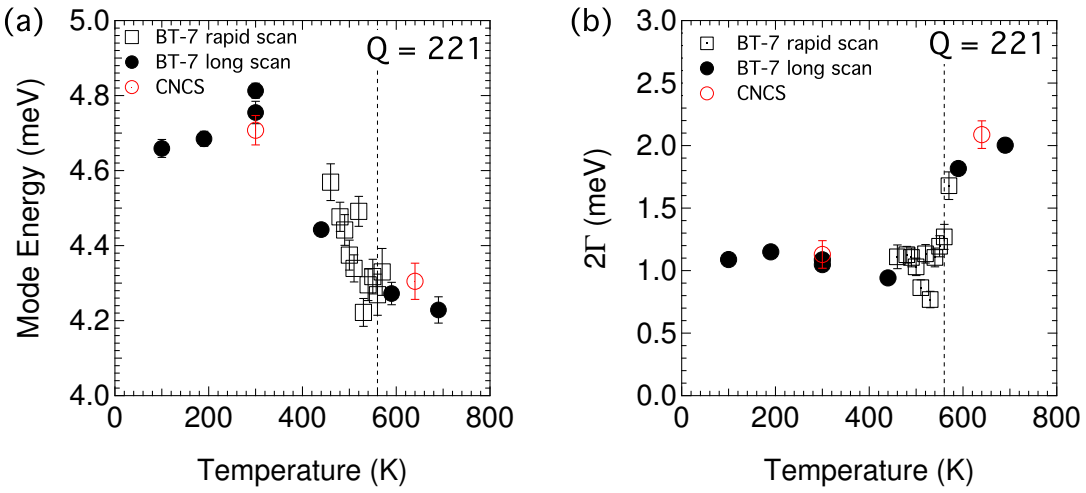

FIG. 6. TA mode energy (a) and phonon scattering rate (b) as a function of temperature on heating derived from constant Q scans at **Q** = (2,2,1) for BT-7 (black markers) and CNCS (red markers) . The measurement point corresponds to the Brillouin zone boundary at the X point in the (00ξ) direction. Fits for BT-7 data are performed in the single mode analysis regime in convolution with the experimental resolution function. Error bars are one standard deviation of the fitting parameter. Vertical dotted line indicates the reported $\beta \rightarrow \gamma$ phase transition temperature of 560 K.

at the X point (reduced phonon wave vector $\mathbf{q} = [0,0,1]$), and the intensity is from the TA mode polarized along $[1,1,0]$. This point provided the most accurate determination of the phonon energy and linewidth, as it corresponds to the relatively flat portion of the TA branch with low group velocity, and is less sensitive to sample mosaic. Results are shown in Fig. 6a comparing BT-7 (black markers) and CNCS measurements (red markers) on heating.The linewidths extracted from INS data are in excellent agreement between the two instruments. Both the energy and linewidth of the TA phonon mode exhibit a dramatic change across the order-disorder phase transition at 560 K. The mode energy is relatively constant at $T \leqslant 300$ K, but exhibits a clear softening of about 10% on warming into the disordered γ phase. The behavior of the phonon linewidth is most striking, with a large step-like increase from ~ 1 meV in the α and β phases to ~ 2 meV upon warming into the γ phase. This represents a doubling of the phonon scattering rate in the cation-disordered γ phase, compared with the long-range ordered β and α phases. We have previously shown in the related $AgSbTe_2$ compound that TA modes dominate thermal transport. This strong increase in phonon scattering rates at the order-disorder transition is thus consistent with the large suppression in thermal conductivity at about 550 K reported in Refs. 11, 12, and consistent with our thermal

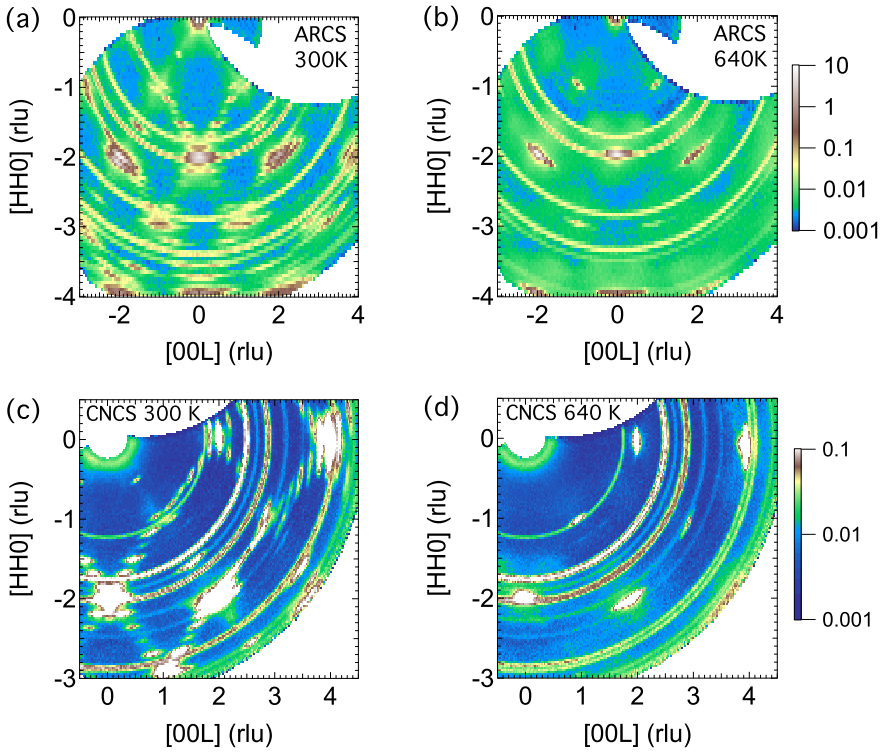

FIG. 7. (color) Elastic intensity measured on $AgBiSe_2$ at (a) 300 K and (b) 640 K in the HHL plane with ARCS (-2 $< E <$ 2 meV), and CNCS at (c) 300 K and (d) 640 K (-1 $< E <$ 1 meV). In all cases, the intensity is integrated over $-0.1 \leq K \leq 0.1$ in the out-of-plane $[K,-K,0]$ direction. The superstructure from long-ranged cation ordering appears as rows of reflections along $\langle 111 \rangle_{\text{cubic}}$ in the trigonal phase at 300 K (a, c), but is absent at 640 K (b, d). At 640 K, patches of diffuse scattering remain, indicative of cation short-ranged order. Diffraction rings are from the polycrystalline Al sample holder, with some sample contributions. Colors are shown on a log scale, and the colorbars from panels (b) and (d) refer to ARCS and CNCS data, respectively.

diffusivity results shown in Fig. 5.

We now discuss the temperature dependent atomic structure of $AgBiSe_2$, probed with both powder neutron diffraction and energy-resolved TOF measurements on single-crystals. Powder diffraction data allow us to track the average crystal structure (ESI). The single-crystal data further reveal weaker diffuse scattering between the Bragg peaks from short-range correlations in the high temperature phase, in addition to long-range ordering observed in the low temperature phase. Fig. 7 shows the elastic diffuse scattering obtained by energy filtering the INS data ($-1 < E <$ 1 meV), revealing diffuse scattering from time-averaged spatial correlations. The energy filtering

allows us to remove the thermal diffuse scattering from phonons, which is an otherwise prominent source of diffuse scattering in this system, similar to the case of $AgSbTe_2$.[18]

Figures 7a and c reveal the development of a superstructure due to the ordering of Ag and Bi cations in the low-T rhombohedral structure (rows of weak reflections along $\langle 111 \rangle_{\text{cubic}}$), in agreement with results from TEM[24], and also observed in our powder neutron diffraction data (ESI). We also observe a longitudinal peak splitting of (222) Bragg peaks due to the symmetry lowering in the low-temperature phase, also in agreement with the powder measurements (ESI). In addition, we note that the multiple possible rhombohedral twin domains appear with equal likelihood, resulting in similar intensities for superstructure peaks along different $\langle 111 \rangle_{\text{cubic}}$ directions. The superstructure Bragg peaks disappear upon heating into the disordered rock salt phase, as demonstrated in Fig. 7b, d. We note that the order-disorder transition was reversible, and reproducible through multiple temperature cycles in the experiments performed on both powders and single-crystals.

Noticeably, diffuse scattering intensity (Fig. 7b,d) remains (along $\langle 111 \rangle_c$) even above T_{od}, revealing retained short-range order. Importantly, the long-range ordering of cations into rhombohedral domains below T_{od} occurred on a relatively fast time scale (within minutes) in our centimeter-size $AgBiSe_2$ sample. This behavior is quite different from our observations in $AgSbTe_2$, which did not become long-range ordered even upon annealing, although the short-range ordering in $AgSbTe_2$ was pronounced and obvious in neutron, x-ray, and electron diffraction[17, 18, 20]. The correlation length for cation short-range order in nominally rock salt $AgSbTe_2$ was estimated to be a few nanometers [17, 18]. To characterize the correlation length in the high-temperature rock salt- γ phase of $AgBiSe_2$, we considered linear cuts of the data along the L direction by integrating the $[HH0]$ axis and fit the resulting broad peaks to Gaussians. The full width half maximum of the diffuse scattering peaks are 0.43(5), and 0.69(5) reciprocal lattice units, thus making them comparable in size to nanoscale correlations observed in $AgSbTe_2$[18]. At temperatures much higher than T_{od}, we expect weakening cation short-range order. We can thus further corroborate our suggestion that the strong increase in phonon scattering at 550 K in Fig. 6b arises from the disordering of Ag/Bi cations on their sublattice, which retains some degree of nanoscale short-range correlations of cations.

The study of thermal conductivity in $AgSbTe_2$ by Morelli *et. al.* pointed to anharmonic scattering suppressing κ_{lat} to the minimum bound theorized by Slack and Cahill[8].

However, sound velocities used in that study were overestimated by a factor of almost three,

compared with recent neutron scattering measurements of acoustic phonon dispersions and resonant-ultrasound measurements [17], leading to a significant overestimation of the minimum $\kappa_{\rm lat}$.

From neutron scattering, x-ray scattering, electron microscopy, and scanning probe microscopy, a short-range ordering of Ag^{+} and Sb^{3+} on the cation sublattice was identified in $AgSbTe_2$[17, 18, 20–23], and this nanometer-scale inhomogeneity was shown to strongly scatter the phonons in a temperature-independent fashion. The short-ranged order and additional point-defects in $AgSbTe_2$ may be the result of structural frustration due to an inherent non-stoichiometry (composition close to $Ag_{22.2}Sb_{26.8}Te_{51}$). On the other hand, $AgBiSe_2$ forms more readily at the stoichiometric composition[16, 59].

The κ we measured in $AgBiSe_2$ is very low (Fig. 8), about 0.68 $\mathrm{Wm^{-1}K^{-1}}$ at 300 K decreasing slowly to 0.46 $\mathrm{Wm^{-1}K^{-1}}$ at 700 K.

Our κ measurements are in good agreement with previous reports obtained on a quenched pseudo-rocksalt sample in the temperature region over which they overlap (300 to 400 K) [8, 60]. The large change in phonon linewidth on warming across the order-disorder transition observed in our INS measurements of $AgBiSe_2$ is expected to directly correlate with a suppression of κ_{lat}. Indeed, our thermal diffusivity measurements show a pronounced suppression in the disordered phase above approximately 550 K (Fig. 5).

To evaluate the importance of different phonon scattering mechanisms in $AgBiSe_2$, we modeled κ_{lat} by incorporating results from our phonon measurements as well as our first-principles simulations. While the total thermal conductivity (κ) is the sum of lattice (κ_{lat}) and electronic (κ_{el}) components, the κ_{el} in $AgBiSe_2$ with rock-salt structure is several orders of magnitude smaller that κ_{lat} due to its very low σ [9], and can be neglected. Consequently, we can compare the simulated κ_{lat} directly with our experimental values (for total κ) in Fig. 8. We consider the impact on $\kappa_{\rm lat}$ from several phonon scattering processes, in particular anharmonicity and scattering by disorder on the cation sublattice [61].

The κ_{lat} is calculated using a standard phenomenological model [61]:

$$\kappa_{lat} = \frac{1}{3}\sum_{\mathbf{q},j} C_{v_{\mathbf{q},j}} v^2_{\mathbf{q},j} \tau_{total_{\mathbf{q},j}} \tag{5}$$

where $C_{v_{\mathbf{q},j}}$, $v_{\mathbf{q},j}$ and $\tau_{total_{\mathbf{q},j}}$ are the mode heat capacity, mode group velocity, and mode total scattering rate, respectively, and indices $\mathbf{q}$ and j denote the phonon wave vector and branch number. Both $C_{v_{\mathbf{q},j}}$ and $v_{\mathbf{q},j}$ were determined by our DFT calculations of phonons based on the harmonic

approximation [55].

Our analysis considers four distinct scattering processes: Umklapp scattering (U), boundary scattering (B), as well as the effect of the random distribution of Ag and Bi on the cation sublattice (for the disordered rocksalt phase only), adding mass (M) and force-constant (FC) disorder:

$$\tau^{-1}_{total_{\mathbf{q},j}} = \tau^{-1}_{U_{\mathbf{q},j}} + \tau^{-1}_{B_{\mathbf{q},j}} + \tau^{-1}_{M_{\mathbf{q},j}} + \tau^{-1}_{FC_{\mathbf{q},j}} \tag{6}$$

The scattering rates are parameterized as follows (mode indices $\mathbf{q}$, j are left implicit):

$$\tau^{-1}_{U} = \frac{\hbar\gamma^2}{Mv^2\theta_D}\omega^2 T^n exp(-\theta_D/bT) \tag{7}$$

$$\tau^{-1}_{B} = v/d \tag{8}$$

$$\tau^{-1}_{M} = \frac{V}{4\pi v^3}\omega^4 \sum_i f_i(\frac{\bar{m}-m_i}{\bar{m}})^2 \tag{9}$$

$$\tau^{-1}_{FC} = \frac{V}{2\pi v^3}\omega^4 \sum_i f_i(\frac{\bar{F}-F_i}{\bar{F}})^2 \tag{10}$$

where $\hbar$ is the reduced Planck constant, γ the Grüneisen parameter, v the group velocity, θ_D the Debye temperature, ω ($E = \hbar\omega$) the phonon frequency, d the grain size, and V the volume per atom. Here, M is the average atom mass and $\bar{F}$ is the average self-force constant. Individual atoms of type i, with fraction f_i, have masses m_i and self-force constants F_i. We also evaluated the disorder scattering with the expressions derived by Maris [62]:

$$\tau^{-1}_{M} = \frac{\pi V\omega^2 D(\omega)}{6}\sum_i f_i(\frac{\bar{m}-m_i}{\bar{m}})^2 \tag{11}$$

$$\tau^{-1}_{FC} = \frac{\pi V\omega^2 D(\omega)}{3}\sum_i f_i(\frac{\bar{F}-F_i}{\bar{F}})^2 \tag{12}$$

where $D(\omega)$ is the phonon density of states per unit volume.

We start by modeling κ_{lat} for the ideal rocksalt system PbSe, which exhibits similar bonding characteristics as $AgBiSe_2$. This was motivated by our previous studies on phonons and thermal transport in $AgSbTe_2$ and PbTe [17, 18, 27], which showed that the ideal rocksalt system PbTe can be considered a virtual crystal approximant of the more complex $AgSbTe_2$ system (isostructural with $AgBiSe_2$), once the phonon frequencies are normalized for the mass effect. We performed harmonic DFT simulations of the PbSe phonon dispersions, and subsequently introduced Umklapp and boundary scattering with the expressions given above. Using quasi-harmonic phonon calculations for PbSe, we obtained an average $\gamma = 2.0$, in agreement with previous estimations of

1.65 and 2.23 [63, 64]. The Debye temperature $\theta_D = 170$ K was estimated by $\frac{4<E>}{3k_B}$ using the LDA phonon spectrum. We set the constant b as $2N^{1/3} = 4$ where N is the atom number in the conventional unit-cell[65]. The constant n was set to 1.2. The larger value than 1 (pure Umklapp processes) can be seen as representing the effect of phonon group velocity renormalization with temperature. As can be seen in Fig. 8, our model for κ_{lat} in PbSe matches the reported experimental values well at high temperature[66, 67]. The larger discrepancy at low temperatures ~~here~~ could result from underestimating anharmonicity or defects (or dopants), as κ_{lat} in PbSe is highly dependent on carrier concentration[68].

Next, to describe the disordered rocksalt phase of $AgBiSe_2$, we include the scattering rates τ_M^{-1} and τ_{FC}^{-1} associated with disorder on the cation sublattice. We introduce this disordered distribution of Ag^+ and Bi^{3+} as a deviation from the VCA model based on PbSe, corrected for average cation mass ($(m_{\text{Ag}} + m_{\text{Bi}})/2$). For $AgBiSe_2$, the reported γ varies from 1.6 [15] to 2.9 [60] which could originate from the error bars in experiments. To avoid introducing extra uncertainty, we kept the same $\gamma = 2$ and $n = 1.2$ as for PbSe. We set $\theta_D = 311$ K based on the mean phonon energy extracted from our $AgBiSe_2$ phonon DOS measurement. The mass of Pb^{2+} is heavier than the average mass of Ag^+ and Bi^{3+}, thus if we simply replace the Pb^{2+} in the VCA with the average mass of Ag^+ and Bi^{3+}, the resulting κ_{lat} is higher than PbSe (ESI Fig. 13). Thus, disorder-induced scattering is quite significant to account for the κ_{lat} suppression in $AgBiSe_2$ compared to PbSe (see Fig. 8). This cation disorder in the high-temperature rocksalt phase is modeled with a 50% occupational disorder of Ag and Bi cations, namely: $f_i = 0.5$ for both Ag and Bi. The atomic masses of Ag and Bi are 107.87 and 208.98 amu, respectively, leading to $\sum_i f_i(\frac{\bar{m}-m_i}{\bar{m}})^2 = 0.102$. For τ_{FC}^{-1}, the self-force constants of Ag and Bi are 2.79 and 5.25 eV/Å^2, respectively (from D_4 LDA harmonic approximation), and $\sum_i f_i(\frac{\bar{F}-F_i}{\bar{F}})^2 = 0.094$. In addition, INS data revealed patches of diffuse scattering above T_{od}, indicating a residual cation short-range ordering over nanometers, providing a source of boundary scattering. Since the boundary scattering rate is directly proportional to the scattering length scale, by assuming 25% scattering chance by the 5 nanometers short-range ordering, an effective boundary scattering length of 20 nm was used. The combined effects of τ_M^{-1}, τ_{FC}^{-1} and τ_B^{-1} significantly suppresses κ_{lat} in disordered $AgBiSe_2$ (Fig. 8 blue line), yielding a result that matches our measurements at high T (green squares) as well as prior reports on quenched samples of the disordered rock salt phase (purple and brown dots)[8, 60].

We similarly estimated κ_{lat} for the ordered $L1_1$ structure, using the phonon dispersions from our quasi-harmonic DFT simulations of the $L1_1$ phase. The boundary scattering length was set

to be 100 nm as observed by TEM [24] and we applied a small fraction of point-defect scattering ($\sum_i f_i(\frac{\bar{m}-m_i}{\bar{m}})^2 = 0.02$). The calculated κ_{lat} for this long-range ordered phase (featuring little cation disorder) roughly follows a $1/T$ behavior for $T > 30$ K, indicating that the dominant scattering process is anharmonic umklapp scattering, as expected. The result is shown in Fig. 8 (orange line) and qualitatively reproduces the trend reported by Nielsen *e*t. al. for the annealed $AgBiSe_2$ samples in the trigonal structure (pink dots). While the agreement for the $L1_1$ ordered phase is only qualitative, our analysis does capture the strong κ_{lat} suppression in the quenched disordered rock-salt phase, especially below 300 K (blue vs orange lines) and the weak temperature dependence in that phase. While the second model of disorder scattering (Maris) gives a slightly larger κ_{lat}, the agreement with experiments remains fair, and the strong suppression upon cation disordering is preserved. Our thermal conductivity analysis thus supports our observations from INS measurements that phonons are strongly scattered by the disordering of Ag^{+} and Bi^{3+} on the cation sublattice.

CONCLUSIONS

In summary, neutron scattering measurements have been carried out to assess the structure and dynamics of $AgBiSe_2$ across the cation order-disorder transition at $T_{\mathrm{od}} \approx 550$K. Substantial changes in phonon scattering rates are observed at the transition, with the extracted TA linewidths doubling upon heating into the high-temperature disordered γ phase, consistent with an observed drop in the measured thermal diffusivity. A static diffuse scattering component is observed in the γ phase near the transition, and can be attributed to remnant short-range ordering of the cations. Thermal conductivity modeling assessing the phonon scattering contributions from umklapp, boundary scattering, and point-defect mechanisms establishes a strong thermal conductivity suppression from the mass- and force-constant disorder on the Ag-Bi cation sublattice, which is directly validated by our neutron scattering results. To our knowledge, these are the first INS measurements on $AgBiSe_2$, and represent the first set of *in-situ* measurements of controlled linewidth change with cation ordering in a thermoelectric compound. This work explicitly highlights the impact of tunable microstructure on phonon scattering rates and thermal conductivity, providing new insights on coupling phonon scattering mechanisms to optimize thermal transport for rational material design.

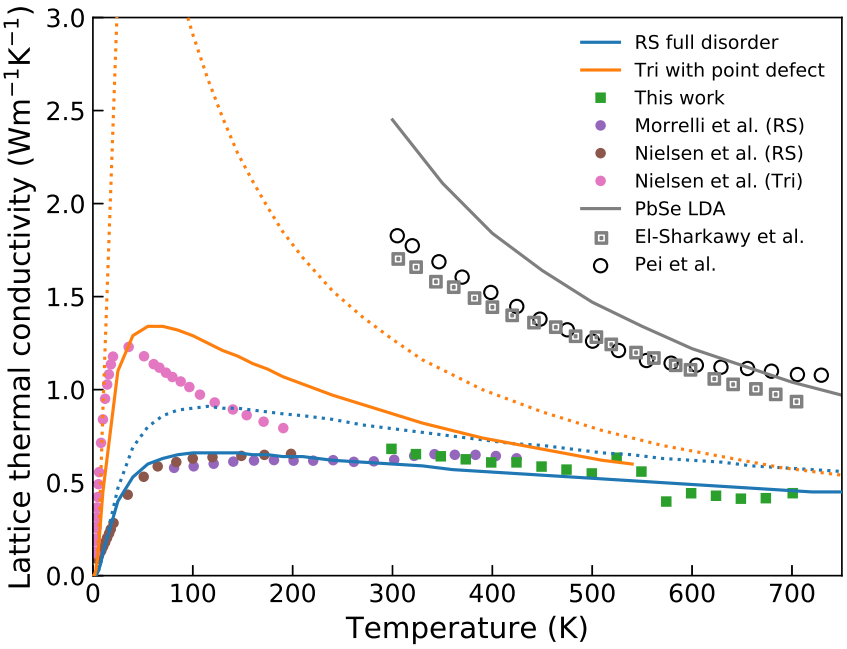

FIG. 8. (color) Comparison of thermal conductivity models and experimental values. Markers represent our κ measurements (green squares), and reported κ for quenched sample with pseudo-rocksalt structure from Morrelli *et. al.* (purple circles) [8] and Nielsen (brown circles) *et. al.* [60], as well as the low-temperature ordered trigonal phase (pink circles) [60]. The κ_L obtained from our phenomenological model for the pseudo-rocksalt structure (see text) is shown as a blue line. The orange line shows κ_L for our model of the ordered $L1_1$ structure (see text). Dotted lines represent a modified point-defect scattering model based on the expressions derived by Maris to take into account the shape of the DOS. The black circles and grey dotted squares show the measured values for PbSe [66, 67], while the grey line represents our PbSe model.

CONTRIBUTIONS

JLN, DB, CWL and OD performed neutron scattering experiments with assistance from DLA, GE, AH, DP, and JWL. JLN analyzed all neutron data, including resolution deconvolution steps. First principles simulations were performed by DB and JD. Sample synthesis was performed by AFM. HW performed the thermal diffusivity measurements. TLA performed heat capacity measurements. Resolution estimation software was written by JYYL. JLN and OD wrote the manuscript with input and review from all authors. OD supervised the project.

ACKNOWLEDGEMENTS

J.N. wishes to acknowledge useful discussions with N.P. Luciano and J. Ma, technical support from D. Dunning, S. Elorfi, and E. Huckabay, and manuscript reviews by L. Lindsey and M. B. Stone. Neutron scattering measurements and analysis (J.N., C.L, O.D.) were supported as part of the S3TEC EFRC, an Energy Frontier Research Center funded by the U.S. Department of Energy, Office of Science, Basic Energy Sciences under Award # DE-SC0001299. First-principles simulations (D.B.) were supported by the U.S. Department of Energy, Office of Science, Basic Energy Sciences, Materials Sciences and Engineering Division, under the Early Career Award No. DE-SC0016166 (PI O.D.) Thermal conductivity modeling (JD) and thermal measurements (TLA) were supported by the U.S. Department of Energy, Office of Science, Basic Energy Sciences, Materials Sciences and Engineering Division, under Award No. DE-SC0019299. Sample synthesis (A.F.M.) was supported by the U. S. Department of Energy, Office of Science, Basic Energy Sciences, Materials Sciences and Engineering Division. H.W. was supported by the Propulsion Materials program of Vehicle Technology Office under EERE. The research at Oak Ridge National Laboratory was sponsored by the Scientific User Facilities Division, Office of Basic Energy Sciences, U. S. Department of Energy. Theoretical calculations were performed using resources of the National Energy Research Scientific Computing Center, a U. S. DOE Office of Science User Facility supported by the Office of Science of the U. S. Department of Energy under Contract No. DE-AC02-05CH11231. We acknowledge the support of the National Institute of Standards and Technology, U.S. Department of Commerce, in providing the neutron research facilities used in this work.

---

* niedzielajl@ornl.gov;

† olivier.delaire@duke.edu

[1] C. Wood, Reports on Progress in Physics **51**, 459 (1988).

[2] G. Chen, M. S. Dresselhaus, G. Dresselhaus, J. P. Fleurial, and T. Caillat, International Materials Reviews **48**, 45 (2003).

[3] G. J. Snyder and E. S. Toberer, Nature Materials **7**, 105 (2008).

[4] H. J. Goldsmid, *Introduction to Thermoelectricity*, Springer Series in Materials Science, Vol. 121 (Springer Berlin Heidelberg, Berlin, Heidelberg, 2010).

[5] J. He and T. M. Tritt, Science **357**, 1369 (2017).

[6] W. Liu, J. Hu, S. Zhang, M. Deng, C.-G. Han, and Y. Liu, Materials Today Physics **1**, 50 (2017).

[7] E. F. Hockings, Journal of Physics and Chemistry of Solids **10**, 341 (1959).

[8] D. T. Morelli, V. Jovovic, and J. P. Heremans, Physical Review Letters **101**, 035901 (2008).

[9] M. D. Nielsen, V. Ozolins, and J. P. Heremans, Energy and Environmental Science **6**, 570 (2013).

[10] K. F. Hsu, S. Loo, F. Guo, W. Chen, J. S. Dyck, C. Uher, T. Hogan, E. K. Polychroniadis, and M. G. Kanatzidis, Science **303**, 818 (2004).

[11] L. Pan, D. Bérardan, and N. Dragoe, Journal of the American Chemical Society **135**, 4914 (2013).

[12] S. N. Guin, V. Srihari, and K. Biswas, Journal of Materials Chemistry A: Materials for Energy and Sustainability **3**, 648 (2014).

[13] C. Xiao, X. Qin, J. Zhang, R. An, J. Xu, K. Li, B. Cao, J. Yang, B. Ye, and Y. Xie, Journal of the American Chemical Society **134**, 18460 (2012).

[14] D. S. Parker, A. F. May, and D. J. Singh, Physical Review Applied **3**, 064003 (2015).

[15] F. Böcher, S. P. Culver, J. Peilstöcker, K. S. Weldert, and W. G. Zeier, Dalton Transactions **46**, 3906 (2017).

[16] S. Mitra and D. Bérardan, Crystal Research and Technology **52**, 1700075 (2017).

[17] J. Ma, O. Delaire, A. F. May, C. E. Carlton, M. A. McGuire, L. H. VanBebber, D. L. Abernathy, G. Ehlers, T. Hong, A. Huq, W. Tian, V. M. Keppens, Y. Shao-Horn, and B. C. Sales, Nature Nanotechnology **8**, 445 (2013).

[18] J. Ma, O. Delaire, E. D. Specht, A. F. May, O. Gourdon, J. D. Budai, M. A. McGuire, T. Hong, D. L. Abernathy, G. Ehlers, and E. Karapetrova, Physical Review B **90**, 134303 (2014).

[19] E. D. Specht, J. Ma, O. Delaire, J. D. Budai, A. F. May, and E. A. Karapetrova, Journal of Electronic Materials **44**, 1536 (2014).

[20] C. E. Carlton, R. De Armas, J. Ma, A. F. May, O. Delaire, and Y. Shao-Horn, Journal of Applied Physics **115**, 144903 (2014).

[21] L. Aggarwal, J. S. Sekhon, S. N. Guin, A. Arora, D. S. Negi, R. Datta, K. Biswas, and G. Sheet, Applied Physics Letters **105**, 113903 (2014).

[22] J. Zhang, X. Qin, D. Li, C. Song, Y. Liu, H. Xin, T. Zou, and Y. Li, Electronic Materials Letters **11**, 133 (2015).

[23] B. Du and X. Tang, Journal of Electronic Materials **44**, 2118 (2015).

[24] C. Manolikas and J. Spyridelis, Materials Research Bulletin **12**, 907 (1977).

[25] S. Geller and J. H. Wernick, Acta Crystallographica **12**, 46 (1959).

[26] A. C. Glatz and A. Pinella, Journal of Materials Science **3**, 498 (1968).

[27] O. Delaire, J. Ma, K. Marty, A. F. May, M. A. McGuire, M.-H. Du, D. J. Singh, A. Podlesnyak, G. Ehlers, M. D. Lumsden, and B. C. Sales, Nature Materials **10**, 614 (2011).

[28] P.-F. Lory, S. Pailhès, V. M. Giordano, H. Euchner, H. D. Nguyen, R. Ramlau, H. Borrmann, M. Schmidt, M. Baitinger, M. Ikeda, P. Tomeš, M. Mihalkovič, C. Allio, M. R. Johnson, H. Schober, Y. Sidis, F. Bourdarot, L. P. Regnault, J. Ollivier, S. Paschen, Y. Grin, and M. Boissieu, Nature Communications **8**, 491 (2017).

[29] J. Y. Y. Lin, H. L. Smith, G. E. Granroth, D. L. Abernathy, M. D. Lumsden, B. Winn, A. A. Aczel, M. Aivazis, and B. Fultz, Nuclear Instruments and Methods in Physics Research Section A: Accelerators, Spectrometers, Detectors and Associated Equipment **810**, 86 (2016).

[30] S. V. Barabash, V. Ozolins, and C. Wolverton, Physical Review Letters **101**, 151 (2008).

[31] G. L. Squires, *Introduction to the Theory of Thermal Neutron Scattering*, 3rd ed. (Cambridge University Press, Cambridge, 2009).

[32] P. Brüesch, *Phonons: Theory and Experiments* (Springer-Verlag, 1982).

[33] G. P. Srivastava, *The Physics of Phonons* (Taylor and Francis, 1990).

[34] A. A. Maradudin and A. E. Fein, Physical Review **128**, 2589 (1962).

[35] R. A. Cowley, Reports on Progress in Physics **31**, 123 (1968).

[36] J. L. Niedziela and et. al, See Supplemental Material at [URL will be inserted by publisher] for additional details on synthesis, characterization, data analysis, and resolution corrections. (2020).

[37] J. W. Lynn, Y. Chen, S. Chang, Y. Zhao, S. Chi, W. Ratcliff II, B. G. Ueland, and R. W. Erwin, Journal of Research of the National Institute of Standards and Technology **117**, 60 (2012).

[38] D. L. Abernathy, M. B. Stone, M. J. Loguillo, M. S. Lucas, O. Delaire, X. Tang, J. Y. Y. Lin, and B. Fultz, Review of Scientific Instruments **83**, 015114 (2012).

[39] G. Ehlers, A. A. Podlesnyak, J. L. Niedziela, E. B. Iverson, and P. E. Sokol, Review of Scientific Instruments **82**, 085108 (2011).

[40] D. L. Abernathy, J. L. Niedziela, and M. B. Stone, EPJ Web of Conferences **83**, 03001 (2015).

[41] M. B. Stone, J. L. Niedziela, M. J. Loguillo, M. A. Overbay, and D. L. Abernathy, Review of Scientific Instruments **85**, 085101 (2014).

[42] M. B. Stone, J. L. Niedziela, M. A. Overbay, and D. L. Abernathy, EPJ Web of Conferences **83**, 03014 (2015).

[43] O. Arnold, J. C. Bilheux, J. M. Borreguero, A. Buts, S. I. Campbell, L. Chapon, M. Doucet, N. Draper, R. Ferraz Leal, M. A. Gigg, V. E. Lynch, A. Markvardsen, D. J. Mikkelson, R. L. Mikkelson, R. Miller, K. Palmen, P. Parker, G. Passos, T. G. Perring, P. F. Peterson, S. Ren, M. A. Reuter, A. T. Savici, J. W. Taylor, R. J. Taylor, R. Tolchenov, W. Zhou, and J. Zikovsky, Nuclear Instruments and Methods in Physics Research Section A: Accelerators, Spectrometers, Detectors and Associated Equipment **764**, 156 (2014).

[44] R. Ewings, A. Buts, M. Le, J. van Duijn, I. Bustinduy, and T. Perring, Nuclear Instruments and Methods in Physics Research Section A: Accelerators, Spectrometers, Detectors and Associated Equipment **834**, 132 (2016).

[45] P. Brüesch, *Phonons: Theory and Experiments I*, Springer Series in Solid-State Sciences, Vol. 34 (Springer Berlin Heidelberg, Berlin, Heidelberg, 1982).

[46] M. B. Stone, J. L. Niedziela, D. L. Abernathy, L. DeBeer-Schmitt, G. Ehlers, O. Garlea, G. E. Granroth, M. Graves-Brook, A. I. Kolesnikov, A. Podlesnyak, and B. Winn, Review of Scientific Instruments **85**, 045113 (2014).

[47] M. Kresch, O. Delaire, R. Stevens, J. Y. Y. Lin, and B. Fultz, Physical Review B **75**, 104301 (2007).

[48] A. Huq, J. P. Hodges, O. Gourdon, and L. Heroux, Zeitsch Kristall Proc (2011).

[49] A. C. Larson and R. B. Von Dreele, *GSAS General Structure Analysis System, Report LAUR 86-748* (Los Alamos National Laboratory, 1986).

[50] G. Kresse and J. Hafner, Physical Review B **47**, 558 (1993).

[51] G. Kresse and J. Furthmüller, Physical Review B **54**, 11169 (1996).

[52] G. Kresse and J. Furthmüller, Computational Materials Science **6**, 15 (1996).

[53] J. Perdew and A. Zunger, Physical Review B **23**, 5048 (1981).

[54] J. Perdew, K. Burke, and M. Ernzerhof, Physical Review Letters **77**, 3865 (1996).

[55] A. Togo and I. Tanaka, Scripta Materialia **108**, 1 (2015).

[56] F. Bao, R. Archibald, J. L. Niedziela, D. Bansal, and O. Delaire, Nanotechnology **27**, 484002 (2016).

[57] M. Popovici, Acta Crystallographica Section A: Crystal Physics, Diffraction, Theoretical and General Crystallography **31**, 507 (1975).

[58] E. Farhi, Y. Debab, and P. Willendrup, Journal of Neutron Research **17**, 5 (2013).

[59] Y. M. Shykhev, Y. A. Yusibov, B. A. Popovkin, and M. B. Babanly, Russian Journal of Inorganic Chemistry **48**, 1941 (2003).

[60] M. D. Nielsen, V. Ozolins, and J. P. Heremans, Energy and Environmental Science **6**, 570 (2013).

[61] T. M. Tritt, *Thermal Conductivity: Theory, Properties, and Applications* (Springer Science and Business Media, 2005).

[62] H. J. Maris, Physical Review B **41**, 9736 (1990).

[63] I. Yu, B. Ravich, and I. Smirnov, "Semiconducting lead chalcogenides," (1970).

[64] Y. Zhang, X. Ke, C. Chen, J. Yang, and P. Kent, Physical Review B **80**, 024304 (2009).

[65] P. Sharma, J. Ahn, N. Hur, S. Park, S. B. Kim, S. Lee, J.-G. Park, S. Guha, and S. Cheong, Physical Review Letters **93**, 177202 (2004).

[66] Y.-L. Pei and Y. Liu, Journal of Alloys and Compounds **514**, 40 (2012).

[67] A. El-Sharkawy, A. A. El-Azm, M. Kenawy, A. Hillal, and H. Abu-Basha, International Journal of Thermophysics **4**, 261 (1983).

[68] H. Wang, Y. Pei, A. D. LaLonde, and G. J. Snyder, Proceedings of the National Academy of Sciences **109**, 9705 (2012).